PAPER

Check for updates

Synergistically enhanced electrical transport properties of SrTiO₃ *via* Fermi level regulation and modulation doping†

Dongmei Li, Dongyang Wang, (iD) Xiao Zhang (iD) * and Li-Dong Zhao (iD) *

SrTiO₃ has gained wide attention as an oxide thermoelectric material due to its high Seebeck coefficient and excellent high-temperature thermal stability. However, its intrinsic insulatory properties hinder its development as a thermoelectric material. Herein, we synergistically improved the electrical transport properties of SrTiO₃ by increasing carrier concentration and maintaining high carrier mobility *via* Fermi level regulation and modulation doping through co-doping and compositing. Nb and La co-doping notably heightened the carrier concentration and regulated the Fermi level in the conduction band, resulting in an enhanced *ZT* value from that of an insulator in SrTiO₃ to 0.033 in $Sr_{0.875}La_{0.125}Ti_{0.85}Nb_{0.15}O_3$ at 923 K. The subsequent TiB₂ compositing simultaneously improved carrier concentration (4.82×10^{17} cm³) and afforded high carrier mobility (3.55×10^4 cm² V⁻¹ S⁻¹) in the $Sr_{0.875}La_{0.125}Ti_{0.85}Nb_{0.15}O_3$ + 4% TiB₂ sample at 923 K. The combination of synergistically improved carrier concentration and retained high carrier mobility resulted in an enhanced power factor (11.04 μW cm⁻¹ K⁻² at 923 K), maximum *ZT* (0.23 at 923 K) and average *ZT* (0.15 at 473–923 K) in $Sr_{0.875}La_{0.125}Ti_{0.85}Nb_{0.15}O_3$ + 4% TiB₂ through co-doping and compositing, which matches those of many excellent SrTiO₃-based materials. Our study demonstrated that the thermoelectric properties of SrTiO₃ could be improved *via* synergistically enhanced electrical transport properties through Fermi level regulation and modulation doping *via* co-doping and compositing, which will inspire further research on SrTiO₃ and other oxide thermoelectric materials with mediocre electrical transport properties.

School of Materials Science and Engineering, Beihang University, Beijing 100191, China. E-mail: zhang_xiao@buaa.edu.cn, zhaolidong@buaa.edu.cn
† Electronic supplementary information (ESI) available. See DOI: 10.1039/d2tc00719c

Dr Xiao Zhang is a postdoctoral research fellow at Beihang University, China. She received her Bachelor of Engineering Degree from the University of Science and Technology, Beijing, in 2013, and received her PhD Degree in Materials Science and Engineering from Beihang University in 2018. She worked at Chongqing University as a faculty staff from 2018 to 2020 before joining Beihang University for postdoctoral research in 2020. Her main research interests focus on thermoelectric materials and devices as well as thermal barrier coatings.

Xiao Zhang

1. Introduction

With the need for green energy, thermoelectric materials have gained growing attention since they can convert heat (industrial waste heat, geothermal heat, *etc.*) into electricity.[1] The conversion efficiency of thermoelectric materials is determined by *ZT*, defined as $ZT = \dfrac{S^2\sigma}{\kappa}T$, where *S*: Seebeck coefficient, *σ*: electrical conductivity, and *κ*: thermal conductivity.[2–5] Through advanced material design and regulatory strategies, the properties of thermoelectric materials have been rapidly developed in recent decades.[6,7] However, most traditional thermoelectric materials comprise expensive elements such as Te[2,8–10] and Ge[1,11] or toxic elements such as S[12,13] and Pb.[14–17] Moreover, the high-temperature resistance and oxidation resistance of traditional thermoelectric materials are mediocre. Therefore, oxide ceramics and oxygenated compounds have been developed for non-toxicity, oxidation resistance, low cost and easy synthesis, satisfying the needs of large-scale production and high-temperature service requirements.[18,19] Compared with other oxide materials, such as $Ca_3Co_4O_9$ and $NaCo_2O_4$, SrTiO₃ (STO) shows superior *S* and excellent thermal stability at high temperatures,[6,20–22] and its isotropic properties indicate good mechanical properties in

This journal is © The Royal Society of Chemistry 2022

J. Mater. Chem. C, 2022, **10**, 13851–13859 | **13851**

Fig. 1 Structural characterization of $SrTiO_3$: (a) structure of the crystal and (b) the atomic orbital resolved electronic band structure. The triple degenerate CBM is located at the Γ point. The right panel shows the Fermi energy surface in the first-Brillouin zone with the isosurface level $E_{CBM} + 0.05$ for these three degenerate bands.

practical applications and a difficulty in fracture in a specific direction, thus gaining more attention as an oxide thermoelectric material.[23,24]

As shown in Fig. 1(a), $SrTiO_3$ has a cubic perovskite structure ($Pm3m$) and a lattice constant of 3.905 Å at room temperature. The valence band maximum (VBM) and conduction band minimum (CBM) are located at the R and Γ points, respectively, indicating that it is an indirect semiconductor with a large band gap of $\sim$1.8 eV (Fig. 1(b)). The VBM mainly originates from the O atom while the CBM mainly results from the Ti-d orbital. Obviously, the CBM is a triple degenerate point and a strong anisotropy of effective mass can be found in the Fermi surface, as shown in the right panel of Fig. 1(b). Additionally, the longitudinal (v_l) and shear (v_s) acoustic velocities, the average sound velocity (v_a) and other elastic properties shown in Table S2 (ESI†) correspond to a high κ for the pristine STO material.

The energy band structure calculation results and the sound velocity measurements showed that the pristine STO material as an insulator has ultralow σ and high κ. Roy et al.[25] reported that the power factor (PF) for Nb-doped $SrTiO_3$ synthesized by spark plasma sintering (SPS) could reach 33.21 μW cm^{-1} K^{-2} at 1229 K. Li et al.[26,27] proved that La doping in STO-Nb (Nb-doped $SrTiO_3$) can not only introduce additional electrons to increase the carrier concentration (n) but also reduce the total energy of the STO-Nb system, effectively increasing the electron-doping efficiency. Besides, Ito et al.[28] found that TiB_2 could enhance the PF, resulting in a ZT_{max} value of $\sim$0.18 for the $Sr_{0.95}Y_{0.05}TiO_3$ + 5 mass% TiB_2 composite. These motivated us to explore the combined role of co-doping and compositing on the thermoelectric properties of STO.

In this work, we optimized the n of a pristine STO insulator by adjusting the Fermi level (E_F) to enter the conduction band

through Nb–La co-doping. In order to further improve the electrical transport, we composited TiB_2, a high electrical conductivity boride, to introduce modulation doping in the STO matrix, synergistically improving n and maintaining high carrier mobility (μ). Therefore, the PF reached an ideal value in the entire investigated temperature range, with $\sim$11.04 μW cm^{-1} K^{-2} for $Sr_{0.875}La_{0.125}Ti_{0.85}Nb_{0.15}O_3$ + 4% TiB_2 at 923 K. Owing to the enhanced electrical transport over the broad temperature range, the $Sr_{0.875}La_{0.125}Ti_{0.85}Nb_{0.15}O_3$ + 4% TiB_2 sample reached a ZT_{max} of $\sim$0.23 at 923 K and an average ZT (ZT_{ave}) of $\sim$0.15 at 473–923 K, revealing the development potential of $SrTiO_3$ for high-temperature thermoelectric applications.

2. Results and discussion

As revealed in Fig. 2, the designed improvement strategy for the thermoelectric performance of STO is divided into two consecutive steps: co-doping and compositing. Firstly, STO was transformed from an insulator to a semiconductor by electron-doping: the B-site (Ti^{4+}) was substituted by Nb^{5+} and the A-site (Sr^{2+}) was substituted by La^{3+}. The experimental results and electronic structure calculations both verify that the La–Nb co-doped STO polycrystal showed measurable σ at room temperature. Secondly, to further synergistically improve n and μ, we composited the optimized La–Nb co-doped STO with TiB_2 with excellent σ. Combining co-doping and compositing, the σ and thermoelectric performance accomplished a striking enhancement in a broad temperature range.

2.1. Transforming STO from an insulator to a semiconductor through increasing carrier concentration via Nb-La co-doping

According to the XRD pattern shown in Fig. 3, the diffraction peaks of all the $SrTi_{1-x}Nb_xO_3$ (x = 0.1, 0.125, 0.15, 0.175)

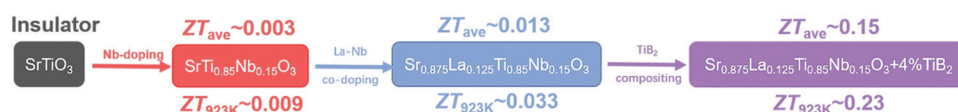**Fig. 2** Roadmap towards the high thermoelectric performance achieved in the $SrTiO_3$-based samples via co-doping and modulation doping.

13852 | J. Mater. Chem. C, 2022, **10**, 13851–13859

This journal is © The Royal Society of Chemistry 2022

Fig. 3 $SrTi_{1-x}Nb_xO_3$ ($x = 0-0.175$): (a) XRD patterns and (b) lattice constant.

Fig. 4 Thermoelectric performance of $SrTi_{1-x}Nb_xO_3$ ($x = 0-0.175$): (a) σ; (b) S; (c) PF; (d) κ_{tot}; (e) κ_{lat}; (f) ZT.

This journal is © The Royal Society of Chemistry 2022

J. Mater. Chem. C, 2022, 10, 13851–13859 | 13853

Fig. 5 Structural characterization of $Sr_{1-y}La_yTi_{0.85}Nb_{0.15}O_3$ ($y = 0-0.15$): (a) XRD patterns and (b) absorption coefficient from the Kubelka−Munk method.

samples matched with the standard PDF card (PDF#35-0734) of STO, indicating that STO-based polycrystals were successfully synthesized by the solid-state reaction (SSR) without any impurity phase. Since the ion radius of Nb^{5+} (0.64 Å) is slightly larger than that of Ti^{4+} (0.61 Å), the lattice constants (Fig. 3(b)) increased gradually with increase in doping content.

Fig. 4 displays the thermoelectric properties of $SrTi_{1-x}Nb_xO_3$, revealing the transformation from insulator to semiconductor at 473–923 K with room-temperature insulativity *via* Nb doping. The σ (Fig. 4(a)) of $SrTi_{1-x}Nb_xO_3$ showed a positive correlation with temperature, and generally increased with increasing

doping content. σ reached ~ 1.9 S cm^{-1} for the $SrTi_{0.85}Nb_{0.15}O_3$ sample at 923 K. Fig. 4(b) shows that the S values of all samples at 473–923 K are negative, indicating that STO can be transformed from an insulator to an n-type semiconductor *via* electron-doping. The absolute values of all S are greater than 280 μV K^{-1}, verifying the development potential of STO due to its high $|S|$ in oxide thermoelectric materials.

The decrease of $|S|$ (absolute value of the Seebeck coefficient) and increase of σ are both due to the increased n *via* electron-doping.[29] Benefiting from the improved σ, the PF of all samples (Fig. 4(c)) shows enhanced electrical transport properties at high

Fig. 6 Electrical transport properties of $Sr_{1-y}La_yTi_{0.85}Nb_{0.15}O_3$ ($y = 0-0.15$): (a) σ; (b) S; (c) PF; (d) μ_W.
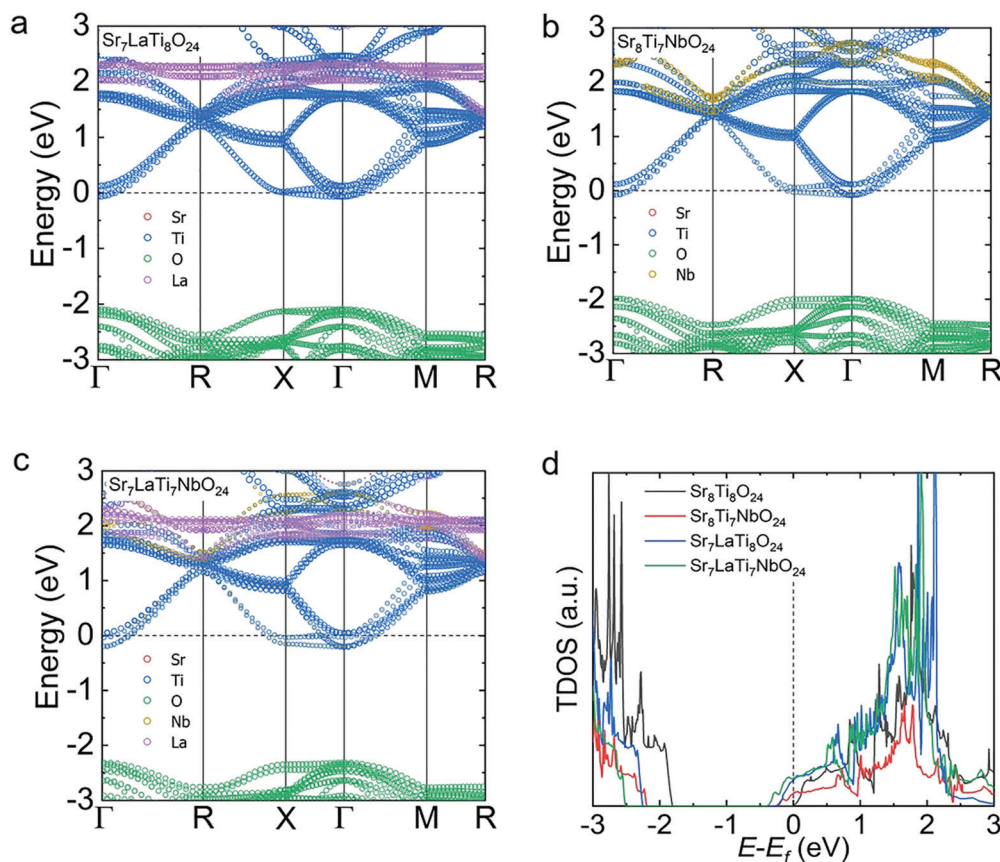
Fig. 7 Electronic band structures and TDOS calculated for the SrTiO₃-based materials: (a) Sr$_7$LaTi$_8$O$_{24}$; (b) Sr$_8$Ti$_7$NbO$_{24}$; (c) Sr$_7$LaTi$_7$NbO$_{24}$; and (d) TDOS near the bottom of the conduction band.

temperatures. The total thermal conductivity (κ_{tot}) (Fig. 4(d)) of the Nb-doped samples is depressed compared with that of un-doped SrTiO₃ due to the enhanced phonon scattering after introducing defects *via* doping.[30,31] The small difference between κ_{tot} and κ_{lat} seen in Fig. 4(e) indicates that lattice vibration is the main mechanism of heat transfer in the SrTi$_{1-x}$Nb$_x$O₃ polycrystal, and that the electrical properties of SrTi$_{1-x}$Nb$_x$O₃ are still inferior. Connected with the simultaneously enhanced electrical transport and depressed thermal properties, the ZT_{max} value (Fig. 4(f)) of SrTi$_{1-x}$Nb$_x$O₃ (x = 0.1, 0.125, 0.15, 0.175) increased from that of an insulator in undoped STO to ∼0.009 for SrTi$_{0.85}$Nb$_{0.15}$O₃ at 923 K, and the ZT_{ave} value (Fig. S2, ESI†) was ∼0.003 for SrTi$_{0.85}$Nb$_{0.15}$O₃ at 473–923 K.

Due to the inferior electrical properties and the room-temperature insulativity of SrTi$_{1-x}$Nb$_x$O₃, La–Nb co-doping was introduced to further increase the electrical transport properties of SrTi$_{0.85}$Nb$_{0.15}$O₃ over a wide temperature range. The XRD patterns of Sr$_{1-y}$La$_y$Ti$_{0.85}$Nb$_{0.15}$O₃ (y = 0, 0.1, 0.125, 0.15) in Fig. 5(a) suggest that the La–Nb co-doped STO purity phase was synthesized. The measured band gap of Sr$_{1-y}$La$_y$Ti$_{0.85}$Nb$_{0.15}$O₃ (Fig. 5(b)) showed a slight increase compared with that of SrTi$_{0.85}$Nb$_{0.15}$O₃, consistent with the theoretical calculation, which will be discussed later.

The σ of the Sr$_{1-y}$La$_y$Ti$_{0.85}$Nb$_{0.15}$O₃ samples (Fig. 6(a)) increased with temperature, reflecting good semiconductor

behavior and did not reach a peak value within the tested temperature range. Besides, the σ values of Sr$_{1-y}$La$_y$Ti$_{0.85}$Nb$_{0.15}$O₃ are significantly superior to those of SrTi$_{0.85}$Nb$_{0.15}$O₃. It is worth noting that the σ of all the La–Nb co-doped samples is measurable at room temperature. All the |S| values indicated that the samples are heavily doped semiconductors, almost linearly proportional to temperature (Fig. 6(b)). Meanwhile, the depressed |S| and enhanced σ for all the La–Nb co-doped samples indicates enhanced n through La and Nb co-doping. Therefore, the PF value (Fig. 6(c)) reached ∼0.9 μW cm^{-1} K^{-2} for the Sr$_{0.875}$La$_{0.125}$Ti$_{0.85}$Nb$_{0.15}$O₃ sample at 923 K. On account of the measured σ and S, we acquired the weighted mobility (μ_W) (Fig. 6(d)) of the La–Nb co-doped STO polycrystal. The μ_W of Sr$_{1-y}$La$_y$Ti$_{0.85}$Nb$_{0.15}$O₃ increased monotonously with increase in temperature, possibly due to the thermal activation of the grain boundary.[32,33]

To further understand the doping effect of Nb and La in STO, first-principles calculations were conducted. Compared with the matrix of STO, the introduction of La or Nb can move the E_F into the conduction band, mainly due to the additional electrons introduced by Nb and La. As a result, the n obviously improved compared with that of pristine STO. It is worth noting that the E_F went further into the conduction band with La–Nb co-doping (Fig. 7(c)), and the band gap increased slightly, in accordance with the measured band gap outcome (Fig. 5(b)).
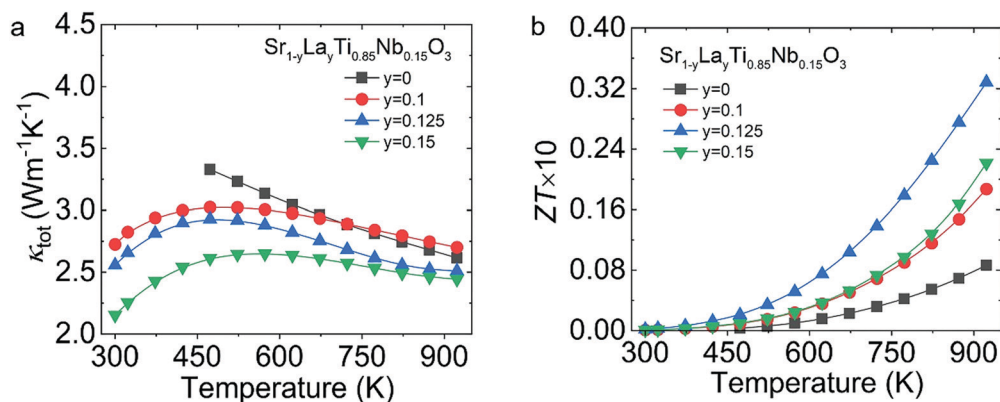
Fig. 8 Thermoelectric transport properties of $Sr_{1-y}La_yTi_{0.85}Nb_{0.15}O_3$ ($y = 0-0.15$): (a) κ_{tot}; (b) ZT.

Fig. 7(d) shows the corresponding total density of states (TDOS) of $Sr_8Ti_8O_{24}$, $Sr_7LaTi_8O_{24}$, $Sr_7LaTi_7NbO_{24}$ and $Sr_7LaTi_7NbO_{24}$, and a clear entrance of E_F into the conduction band in doped systems is observed. The TDOS at the E_F is non-zero regardless of La, Nb and La–Nb co-doping, indicating that the doped material has metallic conductivity.

Fig. 9 Electrical transport properties for $Sr_{0.875}La_{0.125}Ti_{0.85}Nb_{0.15}O_3 + z\%$ TiB_2 ($z = 0-5$): (a) σ; (b) S; (c) PF; (d) n and μ. (e) Modulation-doped semiconductor and (f) regular doped semiconductor.

As displayed in Fig. 8(a), the κ_{tot} for $Sr_{1-y}La_yTi_{0.85}Nb_{0.15}O_3$ showed a negative correlation with La content in the tested temperature range, going from ~ 3.33 W m^{-1} K^{-1} in $SrTi_{0.85}Nb_{0.15}O_3$ to ~ 2.61 W m^{-1} K^{-1} of $Sr_{0.875}La_{0.125}Ti_{0.85}Nb_{0.15}O_3$ at 473 K. The decreased κ_{tot} is due to the intensive phonon scattering by the point defects due to the mass contrast and lattice local strain introduced by co-doping. Benefiting from the enhanced electrical properties and the weakened thermal transport, the ZT_{max} value reached ~ 0.033 at 923 K (Fig. 8(b)).

2.2. Synergistically enhancing the electrical transport of La–Nb co-doped STO through modulation doping via compositing TiB$_2$

To further synergistically enhance the n and μ_W over the entire tested temperature range, we composited $Sr_{0.875}La_{0.125}Ti_{0.85}Nb_{0.15}O_3$ with TiB$_2$, which possesses excellent σ (1×10^5 S cm^{-1}), high melting point (3498 K) and an oxidation resistance temperature in air of 1273 K.[34,35] This afforded an intermetallic compound with a hexagonal graphite-like two-dimensional network structure, where B and Ti atomic planes appear alternately.[36] As depicted in Fig. 9(a), the trend of σ with temperature shows that the semi-conductor behavior gradually weakens and the metallic behavior gradually increases with increase in TiB$_2$ concentration ($z\%$ from 0% to 5%). Particularly, the σ of $Sr_{0.875}La_{0.125}Ti_{0.85}Nb_{0.15}O_3$ with 1% and 2% TiB$_2$ showed monotonic positive correlation with temperature, while the σ of the 3% TiB$_2$ composite increased first and then decreased, and the electrical properties of the 4% and 5% TiB$_2$ composites monotonously decreased with increasing

temperature. Additionally, the S (Fig. 9(b)) decreased from ~ -212 μV K^{-1} for $Sr_{0.875}La_{0.125}Ti_{0.85}Nb_{0.15}O_3$ to ~ -48 μV K^{-1} for $Sr_{0.875}La_{0.125}Ti_{0.85}Nb_{0.15}O_3$ + 4% TiB$_2$ at room temperature, and from ~ -321 μV K^{-1} for $Sr_{0.875}La_{0.125}Ti_{0.85}Nb_{0.15}O_3$ to ~ 128 μV K^{-1} for $Sr_{0.875}La_{0.125}Ti_{0.85}Nb_{0.15}O_3$ + 4% TiB$_2$ at 923 K, indicating the enhancement of electrical transport properties. Therefore, the PF (Fig. 9(c)) of all samples was enhanced over the whole temperature range under investigation, especially for the sample with 4% TiB$_2$ where it reaches the highest value of ~ 11 μW cm^{-1} K^{-2} at ~ 675 K. Fig. 9(d) shows that the introduction of TiB$_2$ could effectively increase the n and the μ_W, leading to optimization of the σ of STO. The synergic optimization of the μ_W and n may be due to modulation doping. The different carrier transport properties of three-dimensional modulation doping models and ordinary high-density doping are shown in Fig. 9(e and f). In regular doping, the high-density carrier concentration would reduce μ due to the increased ionized impurity scattering. Comparatively, modulation doping is composed of a high-density carrier concentration phase and a low-density carrier concentration phase, which could depress the ionized impurity scattering and enhance μ, synergistically improving n and retaining a high μ. The modulation doping method has already been utilized in many thermoelectric systems, such as SnSe,[37] BiCuSeO,[38] p-type SiGe,[39] P-type ZnSb,[40] and n-type TeSb$_2$.[41]

As shown in Fig. 10(a), the electric thermal conductivity (κ_{ele}) of $Sr_{0.875}La_{0.125}Ti_{0.85}Nb_{0.15}O_3$ + $z\%$ TiB$_2$ ($z = 0$–5) exhibited a significant increase with increasing TiB$_2$ content, going from
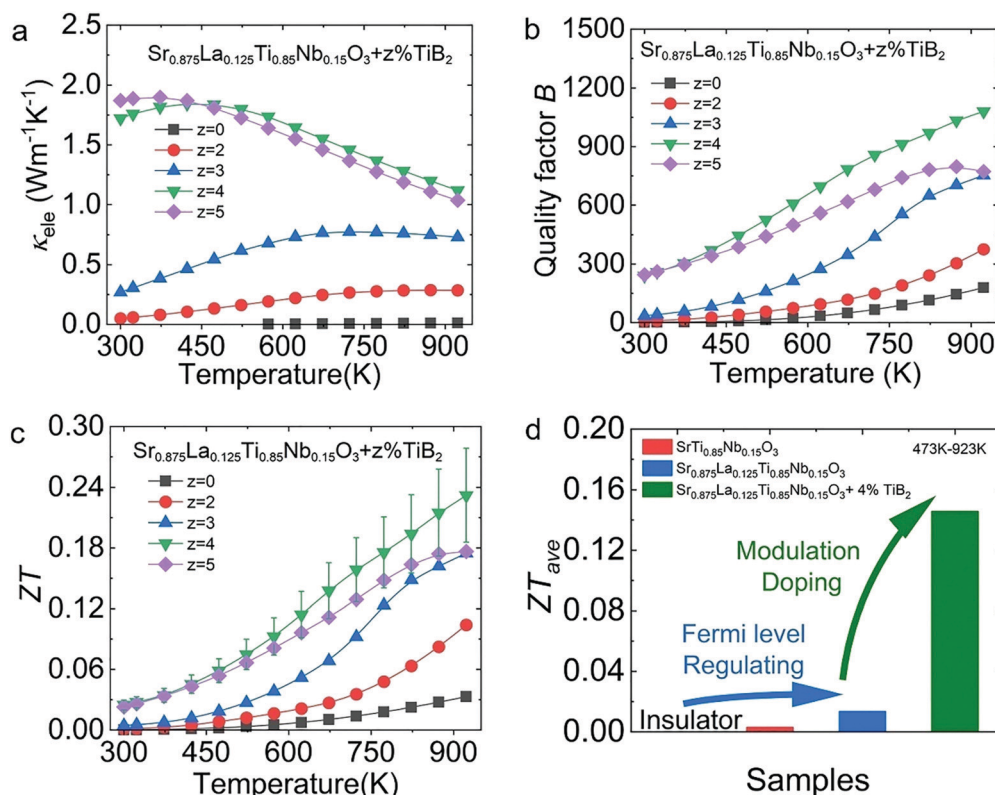

Fig. 10 Thermal transport properties of $Sr_{0.875}La_{0.125}Ti_{0.85}Nb_{0.15}O_3$ + $z\%$ TiB$_2$ ($z = 0$–5): (a) σ; (b) quality factor B; (c) ZT; and (d) average ZT of $SrTi_{0.85}Nb_{0.15}O_3$, $Sr_{0.875}La_{0.125}Ti_{0.85}Nb_{0.15}O_3$ and $Sr_{0.875}La_{0.125}Ti_{0.85}Nb_{0.15}O_3$ + 4% TiB$_2$.
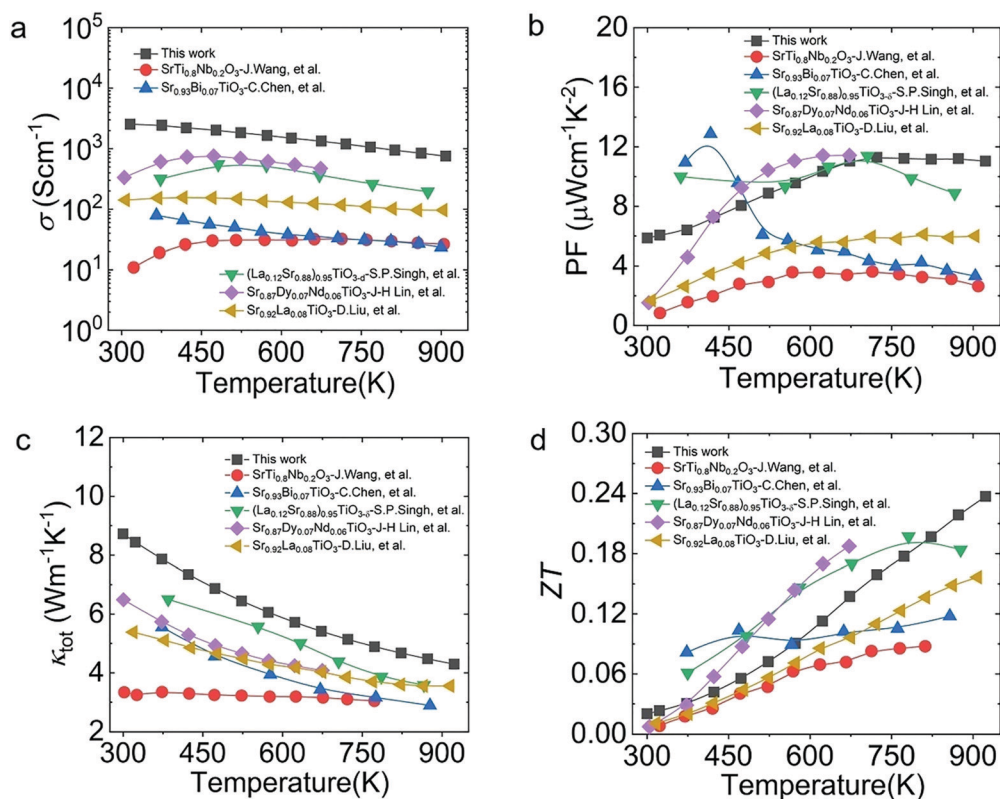
Fig. 11 Thermoelectric properties from this work and from other $SrTiO_3$-based materials: (a) σ; (b) PF; (c) κ_{tot}; (d) ZT.[31,42–45]

~ 0 W m^{-1} K^{-1} in the $Sr_{0.875}La_{0.125}Ti_{0.85}Nb_{0.15}O_3$ sample to ~ 1.72 W m^{-1} K^{-1} in the $Sr_{0.875}La_{0.125}Ti_{0.85}Nb_{0.15}O_3 + 4\%$ TiB$_2$ sample at 300 K. According to Fig. 10(b), the heightened electrical transport properties through modulation doping boost the quality factor (B) of these samples in the tested temperature range. Therefore, the sample with 4% TiB$_2$ obtained a ZT_{max} value of ~ 0.23 at 923 K (Fig. 10(c)), and TiB$_2$ improved the thermoelectric performance of the STO-based materials over the complete tested temperature range. The optimal performance of the Nb-doped, La–Nb co-doped and modulation-doped samples, with ZT_{ave} values of ~ 0.003, ~ 0.013, and ~ 0.15 at 473–923 K, respectively (Fig. 10(d)), showed the significant benefits of the synergetic improvement of n and μ.

We compared the thermoelectric performance of the materials in this work with that of other reported work on STO systems, including $SrTi_{0.8}Nb_{0.2}O_3$,[31] $Sr_{0.93}Bi_{0.07}TiO_3$,[42] $(La_{0.12}Sr_{0.88})_{0.95}$-$TiO_{3-\delta}$,[43] $Sr_{0.87}Dy_{0.07}Nd_{0.06}TiO_3$[44] and $Sr_{0.92}La_{0.08}TiO_3$,[45] as shown in Fig. 11. Due to the significantly heightened σ and PF values over the whole tested temperature range, the ZT_{max} of our work showed strong competitiveness among the STO systems, indicating that STO has the potential to become an excellent thermoelectric material.

3. Conclusion

In this study, the thermoelectric properties of $SrTiO_3$ were gradually enhanced by synergistically improving electrical transport by increasing n and retaining high μ via E_F regulation and modulation doping through co-doping and compositing. Firstly, we introduced Nb doping to adjust the E_F of the pristine STO material to enter the conduction band, transforming it from an insulator to a semiconductor. Secondly, the La–Nb co-doped samples showed obvious semiconductor behavior even at 300 K due to the enhanced n. Thirdly, TiB$_2$ compositing simultaneously improved the n with high μ in $SrTiO_3$ through modulation doping. Therefore, a promising new kind of n-type STO-based polycrystal was obtained through co-doping and compositing, and the ZT_{max} value of $Sr_{0.875}La_{0.125}Ti_{0.85}Nb_{0.15}O_3 +$ 4% TiB$_2$ reached ~ 0.23 at 923 K, with a $ZT_{ave} \sim 0.15$ at 473–923 K. Despite the advancements mentioned above, there is still potential for future research progress, such as reducing thermal conductivity through enhanced phonon scattering.

Conflicts of interest

There are no conflicts of interest to declare.

Acknowledgements

13858 | *J. Mater. Chem. C*, 2022, **10**, 13851–13859

This journal is © The Royal Society of Chemistry 2022

References

1 R. Basu and A. Singh, *Mater. Today Phys.*, 2021, **21**, 100468.

2 G. Tan, W. G. Zeier, F. Shi, P. Wang and M. G. Kanatzidis, *Chem. Mater.*, 2015, **27**, 7801–7811.

3 Z. G. Chen, X. Shi, L. D. Zhao and J. Zou, *Prog. Mater. Sci.*, 2018, **97**, 283–346.

4 X. Y. Liu, D. Y. Wang, H. J. Wu, J. F. Wang, Y. Zhang, G. T. Wang, S. J. Pennycook and L. D. Zhao, *Adv. Funct. Mater.*, 2019, **29**, 1806558.

5 C. Chang, G. J. Tan, J. Q. He, M. G. Kanatzidis and L. D. Zhao, *Chem. Mater.*, 2018, **30**, 7355–7367.

6 X. L. Shi, H. Wu, Q. Liu, W. Zhou and Z. G. Chen, *Nano Energy*, 2020, **78**, 105195.

7 C. Chang, D. Y. Wang, D. S. He, W. K. He, F. Y. Zhu, G. T. Wang, J. Q. He and L. D. Zhao, *Adv. Energy Mater.*, 2019, **9**, 1901334.

8 B. C. Qin, Y. Xiao, Y. M. Zhou and L. D. Zhao, *Rare Met.*, 2018, **37**, 343–350.

9 Y. Xiao, D. Y. Wang, B. C. Qin, J. F. Wang, G. T. Wang and L. D. Zhao, *J. Am. Chem. Soc.*, 2018, **140**, 13097–13102.

10 D. Wu, Y. L. Pei, Z. Wang, H. Wu, L. Huang, L. D. Zhao and J. He, *Adv. Funct. Mater.*, 2014, **24**, 7763–7771.

11 Y. T. Qiu, Y. Jin, D. Y. Wang, M. J. Guan, W. K. He, S. Peng, R. H. Liu, X. Gao and L. D. Zhao, *J. Mater. Chem. A*, 2019, **7**, 26393–26401.

12 W. K. He, D. Y. Wang, J. F. Dong, Y. Qiu, L. W. Fu, Y. Feng, Y. J. Hao, G. T. Wang, J. F. Wang, C. Liu, J. F. Li, J. Q. He and L. D. Zhao, *J. Mater. Chem. A*, 2018, **6**, 10048–10056.

13 Y. L. Pei, H. Wu, J. Sui, L. Jing, D. Berardan, C. Barreteau, P. Lin, N. Dragoe, W. S. Liu and J. He, *Energy Environ. Sci.*, 2013, **6**, 1750–1755.

14 M. Orihashi, Y. Noda, H. T. Kaibe and I. A. Nishida, *Mater. Trans.*, 2007, **39**, 672–678.

15 M. A. Ali, S. A. Dar, A. A. AlObaid, T. I. Al-Muhimeed, H. H. Hegazy, G. Nazir and G. Murtaza, *J. Phys. Chem. Solids*, 2021, **159**, 110258.

16 E. J. Skoug, J. D. Cain and D. T. Morelli, *J. Alloys Compd.*, 2012, **506**, 18–21.

17 X. Qian, H. J. Wu, D. Y. Wang, Y. Zhang, J. F. Wang, G. T. Wang, L. Zheng, S. J. Pennycook and L. D. Zhao, *Energy Environ. Sci.*, 2019, **12**, 1969–1978.

18 X. X. Zhang, C. Chang, Y. Zhou and L. D. Zhao, *Materials*, 2017, **10**, 198.

19 W. W. Qu, X. X. Zhang, B. F. Yuan and L. D. Zhao, *Rare Met.*, 2018, **37**, 79–94.

20 N. M. Ferreira, N. R. Neves, M. C. Ferro, M. A. Torres and A. V. Kovalevsky, *J. Eur. Ceram. Soc.*, 2019, **39**, 4184–4188.

21 C. A. Qi, C. Hnz, B. Yz, A. Hm, C. Xcw and A. Xj, *Ceram. Int.*, 2022, **48**, 9014–9023.

22 Y. Kodama, N. Murayama and Y. T. Yasukawa, *J. Mater. Sci. Lett.*, 1998, **17**, 1999–2001.

23 M. A. Carpenter, C. J. Howard, K. S. Knight and Z. Zhang, *J. Phys.*, 2006, **18**, 10725–10749.

24 M. Guennou, P. Bouvier, J. Kreisel and D. Machon, *Phys. Rev. B: Condens. Matter Mater. Phys.*, 2010, **81**, 054115.

25 P. Roy, V. Pal and T. Maiti, *Ceram. Int.*, 2017, **43**, 12809–12813.

26 Y. Miao, L. Liu, C. Y. Fang, C. Qiqige and A. Wang, *J. Alloys Compd.*, 2016, **665**, 7–12.

27 J. Wang, B. Y. Zhang, H. J. Kang, L. Yan and L. D. Zhao, *Nano Energy*, 2017, **35**, 387–395.

28 O. Naoto and I. Mikio, *Composites, Part B*, 2016, **88B**, 108–113.

29 H. Muta, K. Kurosaki and S. Yamanaka, *J. Alloys Compd.*, 2003, **350**, 292–295.

30 N. Wang, H. Chen, H. He, W. Norimatsu, M. Kusunoki and K. Koumoto, *Sci. Rep.*, 2013, **3**, 3449.

31 J. Wang, X. X. Ye, X. B. Yaer, B. Y. Zhang, W. Ma and L. Miao, *Scr. Mater.*, 2015, **99**, 25–28.

32 W. K. He, B. C. Qin and L. D. Zhao, *Chin. Phys.*, 2020, **37**, 087104.

33 G. J. Snyder, A. H. Snyder, M. Wood, R. Gurunathan, B. H. Snyder and C. Niu, *Adv. Mater.*, 2020, **32**, 2001537.

34 X. Zhang, Z. Zhang, W. Wang, J. Shan, H. Che, J. Mu and G. Wang, *J. Am. Ceram. Soc.*, 2017, **100**, 3099–3107.

35 S. Song, T. Zhang, C. Xie, J. Zhou, R. Li and Q. Zhen, *J. Am. Ceram. Soc.*, 2020, **103**, 719–723.

36 O. Popov, T. Avramenko and V. Vishnyakov, *Mater. Today Commun.*, 2020, **26**, 101756.

37 L. D. Zhao, S. H. Lo, Y. Zhang, H. Sun, G. Tan, C. Uher, C. Wolverton, V. P. Dravid and M. G. Kanatzidis, *Nature*, 2014, **508**, 373–377.

38 Y. L. Pei, H. Wu, D. Wu, F. Zheng and J. He, *J. Am. Chem. Soc.*, 2014, **136**, 13902–13908.

39 B. Yu, M. Zebarjadi, H. Wang, K. Lukas, H. Wang, D. Wang, C. Opeil, M. Dresselhaus, G. Chen and Z. Ren, *Nano Lett.*, 2012, **12**, 2077–2082.

40 M. Amsler, S. Goedecker, W. G. Zeier, G. J. Snyder, C. Wolverton and L. Chaput, *Chem. Mater.*, 2016, **28**, 2912–2920.

41 M. Koirala, H. Zhao, M. Pokharel, S. Chen and T. Dahal, *Appl. Phys. Lett.*, 2013, **102**, 213111.

42 C. Cong, A. Mb, A. Fg and A. Fd, *J. Materiomics*, 2019, **5**, 88–93.

43 S. P. Singh, N. Kanas, T. D. Desissa, M. Johnsson and K. Wiik, *J. Eur. Ceram. Soc.*, 2019, **40**, 401–407.

44 J. H. Lin, C. S. Hwang and F. R. Sie, *Mater. Res. Bull.*, 2020, **122**, 110650.110651–110650.110658.

45 D. Liu, Y. Zhang, H. Kang, J. Li, Z. Chen and T. Wang, *J. Eur. Ceram. Soc.*, 2018, **38**, 807–811.